Hydrogen relative permeability modeling: applications to underground hydrogen storage (UHS)

by

Deborah Olabisi Agbamu

B.Sc., University of Lagos, 2017

A THESIS

submitted in partial fulfillment of the requirements for the degree

MASTER OF SCIENCE

Department of Geology
College of Arts and Sciences

KANSAS STATE UNIVERSITY
Manhattan, Kansas

2025

Approved by:

Co-Major Professor
Dr. Abdelmoneam Raef

Approved by:

Co-Major Professor
Dr. Behzad Ghanbarian

Copyright

Abstract

The transition toward a low-carbon energy system has intensified interest in underground hydrogen storage (UHS) as a means to balance the intermittent nature of renewable energy sources. The accurate modeling of hydrogen flow in subsurface porous media is crucial for optimizing storage efficiency and ensuring successful retrieval. A key parameter in this process is hydrogen relative permeability (k_{rh}), which governs multiphase flow dynamics in geological formations. In this study, we develop a theoretical model for k_{rh} using the effective-medium approximation (EMA) and percolation theory (PT) concepts. Our model incorporates pore-scale characteristics such as pore size distribution, connectivity, and critical hydrogen saturation S_{hc}. The model is validated against eight experimental datasets and eleven pore-network simulations, demonstrating reasonable agreement in most cases. However, discrepancies are observed in certain carbonate samples, likely due to secondary porosity effects (e.g., vugs and fractures) and in sandstones with possible microfractures. The findings highlight the critical role of accurately estimating S_{hc} in predicting k_{rh} and suggest that improvements in pore structure characterization could enhance modeling accuracy.

Table of Contents

List of Figures

List of Tables

Acknowledgements

Firstly, my sincere gratitude goes to my co-major advisors, Dr. Behzad Ghanbarian and Dr. Abdelmoneam Raef. Dr. Ghanbarian's expert guidance, unwavering support, and consistent encouragement have been invaluable throughout the course of this research. His belief in me and persistent push for excellence have profoundly shaped my journey in this program. Dr. Raef's thoughtful critiques and meaningful contributions are not trivial.

Special thanks to Dr. Shaina Kelly of Columbia University for graciously serving on my committee and offering insightful feedback that helped enrich this research.

With deep appreciation, I acknowledge the profound impact of my esteemed course instructors: Dr. Karin Goldberg, Dr. Matthew Kirk, Dr. Claudia Adam, Dr. Abdelmoneam Raef, and Dr. Behzad Ghanbarian. Their dedication to teaching not only expanded my knowledge but also fostered a supportive and familial learning environment that made my time in the department truly worthwhile. I am also grateful to Dr. Pamela Kempton for her salient guidance at a time I needed it most.

I am thankful to the Department of Geology for financial support and providing opportunities for growth and learning.

I also deeply appreciate my inner circle of friends — Matilda King and Nelsy Osorio — for their cherished companionship during this journey.

Many thanks to Victor Oladoja, Luqman Olawale, Tochukwu Onyebum, Fidelis Onwuagba, Kehinde Bosikun, Shaluka Seneverathna, Connor Saari, Emmanuel Gyasi, and Chinedu Okolo for helping to shape this journey.

Much appreciation to the following associations for helping with financial support: American Association of Petroleum Geologists (AAPG), National Association of Black

Geoscientists (NABG), Association for Women Geoscientists (AWG), Association of Earth Science Clubs of Greater Kansas City (AESC), Kansas Geological Foundation (KGF), K-State Graduate School and Arts and Sciences.

I acknowledge the use of ChatGPT-4 for language editing and proofreading of this thesis. The AI was used to improve grammar, clarity, and readability. All intellectual contributions, data interpretation, and conclusions are entirely the work of the author.

Finally, I give all glory to God Almighty (the First and the Last) for without Him, none of this would have been possible.

Dedication

I dedicate this work to my loving husband, Joshua, and our precious son, John. Your unwavering love, patience, and support have been my greatest source of strength. You both are the best part of this journey.

Chapter 1 - Introduction

Hydrogen storage is a viable storage method for renewable energy because hydrogen can be stored in aquifers, depleted hydrocarbon reservoirs, or salt caverns [1]. Subsurface porous media are feasible and abundant options for long-term and large-scale storage of hydrogen underground [2,3]. While hydrogen storage in salt caverns offers the advantage of high purity due to minimal contamination risk, their limited scale and availability make them insufficient to meet the entire storage demand. Therefore, porous reservoirs are considered more widespread and abundant to provide the necessary volumetric capacity for larger-scale UHS, though with a lower degree of purity. Operational costs are also significantly reduced since most sites had prior exploration facilities. UHS is also part of the "Power to Gas" concept that involves converting surplus electricity into hydrogen gas through electrolysis [4], after which it is injected into underground reservoirs for storage or introduced into the gas distribution network through blending or additional conversion to methane.

However, despite the increase in popularity of the UHS, storage mechanisms within subsurface porous media have remained inadequately understood. The need to understand the flow of hydrogen relative to the in-situ fluids during injection is very crucial. This will help construct large-scale hydrogen models on a field basis. This study focuses on the relative permeability of hydrogen as applicable to the UHS.

Relative permeability describes the flowability of a fluid in the presence of other fluids; in this case, the flowability of hydrogen in the presence of water. The relative permeability serves as a critical parameter for numerical modeling of UHS at the field scale, as highlighted in studies by Kanaani et al.[5], Lysyy et al. [6], and Wang et al. [7]. Laboratory gas-water relative permeability curves often exhibit low endpoint gas saturations (<65%) and relative permeabilities (<40%) due

to factors, such as rock heterogeneity, capillary end effects, gravity segregation, and/or maximum experimental capillary pressure, as identified by Krevor et al. [8] and Müller [9]. Consequently, numerical and/or analytical models are essential for the validation and extrapolation [8,10] of relative permeability across a broader saturation range.

One of the most widely used models is the Corey model [11] which expresses relative permeability as a power-law function of normalized saturation. The Corey model is advantageous due to its simplicity and empirical fit to many datasets, but it lacks the ability to account for fluid trapping. The Brooks-Corey model [12] introduced the concept of pore-size distribution in capillary pressure and relative permeability relationships, improving predictions in water-wet reservoirs. However, like the Corey model, it does not explicitly model phase entrapment. Krevor et al. [8] improved CO_2 relative permeability by capturing capillary trapping behavior and this was applied by Bo et al. [13] who demonstrated that this modification to the Brooks-Corey model [8] provides better agreement with experimental results compared to Feldman et al.'s dual permeability modification [14] and equivalent van Genuchten model obtained using the technique introduced by Lenhard et al. [10]

The van Genuchten model [15] improved capillary pressure and relative permeability estimations by introducing a more flexible function to fit experimental data, particularly in unsaturated flow systems. While effective for soil physics applications, its adaptability to petroleum and gas storage scenarios remains a challenge. Similarly, the Burdine and Mualem models [16] provided permeability-saturation relationships based on statistical pore network theories, which improved theoretical consistency but required accurate capillary pressure measurements, often unavailable in field-scale studies.

To address some of these limitations, Parker et al. [17] introduced a semi-empirical model that incorporates hysteresis and non-wetting phase entrapment. Unlike traditional models that assume a single relative permeability curve for both drainage and imbibition, the Parker et al. model [17] accounts for the history-dependent behavior of multiphase flow. This is particularly useful for applications such as gas entrapment in aquifers, CO_2 sequestration, and UHS, where fluid displacement history significantly influences permeability. The model also introduces a trapped non-wetting phase saturation function, which helps predict irreducible gas saturation, making it valuable for assessing residual hydrogen or CO_2 retention in porous media. However, despite these advancements, the Parker et al. [17] model remains empirically driven, requiring extensive calibration, and does not explicitly represent pore-scale dynamics such as film flow or wettability alteration.

More recent studies have revisited and refined these models to enhance their applicability to contemporary subsurface challenges;

For instance, Zheng et al. [18] conducted a sensitivity analysis on relative permeability curves in CO_2 core flooding simulations, comparing the Corey, Brooks-Corey, and van Genuchten models. Their findings indicated that while the Corey and Brooks-Corey models provided consistent predictions, the van Genuchten model yielded significantly different results, highlighting the importance of model selection in accurately simulating CO_2 sequestration processes.

Ogolo et al. [19] emphasized the importance of laboratory-derived relative permeability data, demonstrating that even slight inaccuracies in Corey model exponents can significantly impact reservoir simulations. Their study underscores the necessity of precise calibration of these models to specific reservoir conditions to ensure accurate predictions.

Picchi and Battiato [20] proposed a semi-empirical model that integrates pore-scale flow regimes into the traditional Corey and Brooks-Corey frameworks. Their approach accounts for capillary and viscous limits, offering improved predictions of relative permeabilities across various fluid systems.

These contemporary studies highlight the enduring relevance of classical relative permeability models while advocating for their careful calibration and, when necessary, integration with newer methodologies to address the complexities of modern subsurface applications. The development of advanced relative permeability models continues to be an area of active research, particularly for UHS applications. Hydrogen, due to its low viscosity, high diffusivity, and unique interfacial properties, poses additional complexities that may not be fully captured by traditional models.

This study aims to advance the current understanding of hydrogen flow behavior through the following objectives: (1) applying Poiseuille's law to estimate hydrogen flow at the pore scale, (2) upscaling flow using the EMA and universal power-law scaling from PT, and (3) comparing model predictions with simulations and experimental measurements.

Chapter 2 - Theoretical Modeling of Hydrogen Relative Permeability

In this section, we explain the theoretical approach developed to model the hydrogen relative permeability.

2.1. Hydraulic properties at the pore scale

For a cylindrical pore, the Laplace equation relates the pore size to the capillary pressure as follows

$$r = \frac{4\gamma cos\theta}{P_c} \quad (1)$$

where r represents the pore radius, γ is the interfacial tension (N/m) between two fluids (e.g., mercury-air, water-hydrogen), θ denotes the contact angle (°) between fluid and solid surface, and P_c is the capillary pressure (Pa).

The hydraulic conductance g of such a pore with length l, filled with hydrogen gas of viscosity μ, is given by Poiseuille's law

$$g = \frac{\pi r^4}{8\mu l} \quad (2)$$

2.2. Upscaling from pore to core

The effective-medium approximation (EMA) is an upscaling technique from statistical physics, offering a means to model flow and transport in systems characterized by relatively heterogeneous structures. This approach, has been effectively utilized in the literature for the investigation of diverse petrophysical properties by Ghanbarian et al. [21], Ghanbarian & Javadpour [22], and Richesson & Sahimi[23]. Within the EMA framework, a heterogeneous medium featuring a specific pore conductance distribution $f(g)$ is substituted with a hypothetically homogeneous network where all pores possess an effective pore conductance g_e the determination of which involves solving Equation (3).

$$\int \frac{g_e - g}{g + \left[\frac{Z}{2} - 1\right] g_e} f(g) dg = 0 \quad (3)$$

where Z is the average pore coordination number. In practical applications, Z can be determined from either 3D images [24] or nitrogen sorption isotherms [25]. However, a practical approximation is to set $Z = 2/S_{gc}$, where S_{gc} represents the critical gas saturation for percolation [26]. Consequently, Equation (3) transforms to:

$$\int \frac{g_e - g}{g + \left[\frac{1 - S_{gc}}{S_{gc}}\right] g_e} f(g) dg = 0 \quad (4)$$

Another upscaling technique is the universal power-law scaling from percolation theory (PT) providing a mathematical framework for understanding connected clusters in random networks. In porous media, it quantifies how the interconnectivity of pore spaces influences flow and transport properties [27]. The theory describes how k_{rh} depends on the connected saturation S_h. Below a critical saturation S_{hc}, there is no macroscopic flow.

$$k_{rh} \sim (S_h - S_{hc})^t \quad (5)$$

Above S_{hc}, near the percolation threshold, transport coefficients follow a power law scaling, with the percolation scaling exponent, *t* being 2 for three-dimensional systems. The parameter S_{hc} is non-universal and depends on pore connectivity and fluid-wetting characteristics.

Hydrogen transport at the network level can be scaled up from pore-scale properties, considering pore size distribution and connectivity. Actual pore-throat size distribution is utilized, and the hydraulic pore conductance distribution is derived from $f(g)dg = f(r)dr$. Hydrogen saturation S_h corresponding to pore radius r is determined as follows [21]:

$$\frac{S_h - S_{hr}}{1 - S_{hr}} = \frac{\int_r^{r_{max}} r^3 f(r) dr}{\int_{r_{min}}^{r_{max}} r^3 f(r) dr} \quad (6)$$

where S_{hr} is the residual hydrogen saturation. To enhance our model's prediction [28], we applied the Fredlund and Xing [29]method to estimate the maximum pore radius r_{max}. This was done by

fitting a tangent line at the inflection point on the capillary pressure curve and, which was then extrapolated to the point of full water saturation ($S_w = 1$). The resulting entry pressure was used to calculate r_{max} through the Young-Laplace equation.

Under full saturation conditions ($S_h = 1$), the effective conductance g_e is determined by integrating the conductance distribution.

$$\int_{g_{min}}^{g_{max}} \frac{g_e(S_h=1)-g}{g+\left[\frac{1-S_{hc}}{S_{hc}}\right]g_e(S_h=1)} f(g)dg = 0 \quad (7)$$

where S_{hc} is the critical hydrogen saturation.

Under partial saturation conditions:

$$\int_{g_{min}}^{g} \frac{g_e(S_h)-0}{0+\left[\frac{1-S_{hc}}{S_{hc}}\right]g_e(S_h)} f(g)dg + \int_{g}^{g_{max}} \frac{g_e(S_h)-g}{g+\left[\frac{1-S_{hc}}{S_{hc}}\right]g_e(S_h)} f(g)dg = 0 \quad (8)$$

The values of $g_{\mathrm{e}}(S_{\mathrm{h}} = 1)$ and $g_{\mathrm{e}}(S_{\mathrm{h}})$ are obtained by numerically solving Equations (7) and (8), respectively. To examine the saturation-dependent behavior of hydrogen permeability, $g_{\mathrm{e}}(S_{\mathrm{h}})$ is computed at different S_{h} values. Given that gas permeability is proportional to the effective conductance [30], we define k_{rh} as

$$k_{rh} = \frac{k_h(S_h)}{k_h(S_h=1)} = \frac{g_e(S_h)}{g_e(S_h=1)}. \quad (9)$$

Theoretically, k_{rh} should approach zero as S_h tends to its critical value S_{hc}. It is known that the EMA scaling is not accurate near the critical point [27]. We therefore apply the EMA at high to intermediate hydrogen saturations and employ the universal power-law scaling from PT at low hydrogen saturations near S_{hc}. The crossover between the two occurs at a specific hydrogen saturation S_{hx}. The universal power-law scaling from percolation theory is expressed by Equation (10), where the scaling exponent t is dimension-dependent (1.3 for two dimensions, 2 for three dimensions), and k_0 is a numerical prefactor.

$$k_{rh} = k_0(S_h - S_{hc})^t, \; S_h > S_{hc} \quad (10)$$

The value of k_0 is determined by equating the expressions in Equations (9) and (10) at S_{hx}, where the first derivatives of the two equations are equal. Numerical computations are employed, involving interpolation of estimated k_{rh} values and calculating k_0 and slope at each point. S_{hx} corresponds to the hydrogen saturation at which the slopes of Equations. (9) and (10) are equal.

Chapter 3 - Data

The database used in this study to evaluate our k_{rh} model consists of eight experiments and eleven pore-network models (PNM) which provided drainage hydrogen-brine capillary pressure (CP) or mercury intrusion capillary (MICP) measurements from which pore-throat size distribution (PSD) was obtained. For two datasets, PSD was captured from CT_image and dry scan images. Salient information for all the datasets is shown in Table 1. Each dataset is briefly described, and detailed information can be found in the original publications.

Table 3-1 Information on the nineteen datasets used in this study.

Reference	Sample	Remarks	Porosity (%)	S_{hc} (Frac)			PSD Source			Simulation	Experiment
				Estimated		Measured	CP	MICP	CT image		
				MICP	CP						
Yekta et al. [31]	Buntsandstein Sandstone	Shallow	19	0.31	0.42	0.1	✓	✓	x	x	Steady-state
		Deep	19	0.44	0.42	0.18	✓			x	Steady-state
Hashemi et al. [32]	Berea*	Berea	18	N/A	0.2	0.2	✓	x	x	PNM	x
	Berea	Berea (small)	20	N/A	0.25	0.3	✓	x	x	PNM	x
	A1	Sandstone	43	N/A	0.2	0.2	✓	x	x	PNM	x
	C1	Carbonate	25	N/A	0.06	0.06	✓	x	x	PNM	x
	C2	Carbonate	16	N/A	0.35	0.35	✓	x	x	PNM	x
Rezaei et al. [33]	S1	Sandstone	16	0.09	N/A	0.0015	x	✓	x	x	Unsteady state
	S2	Sandstone	11	0.2	N/A	0.009	x	✓	x	x	Unsteady state
	C1	Carbonate	13	0.15	N/A	0.003	x	✓	x	x	Unsteady state
Boon & Hajibeygi [34]	Berea	Sandstone	20	0.31	0.4	0.04	✓	✓	x	x	Steady-state
Higgs et al. [35]	Bentheimer	Sandstone	23	0.46	N/A	0.46	x	✓	✓	x	Steady-state
Zhao et al. [36]	S1 SCA	Sandstone	25	N/A	0.31	0.06	✓	x	x	PNM	x
	S1 LCA	Sandstone	25	N/A	0.31	0.05	✓	x	x	PNM	x
	S2	Sandstone	17	N/A	0.25	0.6	✓	x	x	PNM	x
	S3	Sandstone	17	N/A	0.5	0.2	✓	x	x	PNM	x
	S7	Sandstone	34	N/A	0.36	0.13	✓	x	x	PNM	x
	BG	Bandera Gray sandstone	21	N/A	0.07	0.07	✓	x	x	PNM	x
Manoorkar et al. [37]	Carbonate	Fractured rock	1	N/A	N/A	0.08	x	x	✓	x	Steady-state

3.1 Experiments

- Yekta et al. (2018)

They obtained Triassic sandstone samples from the Buntsandstein Formation in France. Experiments were conducted for shallow $(20℃, 55\ \text{bar})$ and deeper $(45℃, 100\ \text{bar})$ aquifer conditions. The reported porosity is 0.19 from mercury intrusion porosimetry, with adjustments made for surface roughness and irregularities. A modified semi-dynamic technique was combined with the mercury intrusion capillary pressure (MICP) method to derive capillary pressure evolution for the hydrogen–water system over the entire water saturation range measurements. The interfacial tension values ($\cos\theta = 0.93$ and $\cos\theta = 0.82$) and contact angles (0.051 and 0.046 N/m) for the hydrogen–water system were determined under conditions relevant to UHS. k_{rh} was determined using the conventional steady-state approach, and data were extended to low saturations using capillary pressure measurements, while water saturation measurements utilized the mass balance method. Pore size distribution was obtained from hydrogen-brine capillary pressure curve using the Laplace equation and S_{gc} from the inflection point of the curve.

- Rezaei et al. (2022)

Two sandstones and one carbonate rock samples from gas reservoirs, underwent displacement tests. The mineralogy and pore structures were analyzed through XRD analysis, MICP experiments, and a centrifuge capillary pressure test. They conducted experimental assessments to determine the relative permeability of hydrogen-brine across various conditions showing the impacts of pressure, salinity, rock type (sandstone and carbonate), and gas type (H_2, N_2, and CH_4). We determined pore size distribution from the inflection point on the MICP curve. Our focus was on modeling hydrogen-brine relative permeabilities in the three rock samples.

- Boon & Hajibeygi (2022)

They used a hydrogen-water multi-phase flow experiment conducted on a heterogeneous Berea Sandstone rock to obtain both drainage and imbibition relative permeability and capillary pressure data. The study performed steady-state drainage and imbibition core-flooding experiments, visualizing the transport of hydrogen and brine using a medical X-ray CT scanner. The capillary pressure measurements were combined with MICP data to derive a receding contact angle for the H_2/water/sandstone rock system. In our work, we focused on the drainage data for our model and derived pore size distribution for both H_2/water capillary pressure and MICP measurements.

- Higgs et al. (2024)

The authors measured k_{rh} hysteresis during co-injection core floods of hydrogen and water in the Bentheimer sandstone. The core sample used has a porosity of 23% and an absolute permeability of 653 mD. Experiments were carried out at 298 K and 2.133 MPa with hydrogen viscosity of 0.00891 mPa.s and density of 1.7141 kg/m^3. The interfacial tension (IFT) of the hydrogen-water-quartz system under these conditions is around 72.0 mN/m. Capillary pressure and its relationship with saturation were obtained from MICP. Micro-CT images were used to obtain saturation levels and pore size distribution. The experiment involved using two pumps to inject DI water and pure hydrogen into a flowline, with pressure measured using transducers. Confining pressure was maintained at 6.21 MPa, and a back pressure regulator constrained pore pressure close to 2.13 MPa. Fractional flow of hydrogen was increased incrementally to determine irreducible water, then decreased to determine residual gas. Relative permeability of each phase in the two-phase system was determined as a function of saturation.

- Manoorkar et al. (2024)

Using steady-state experiments at 10 MPa on samples from the Loenhout natural gas storage site in Belgium, the authors measured gas-brine flow behavior and phase interference of hydrogen, methane, and nitrogen within μm-to-mm scale fractures. Aperture distribution was obtained from segmented dry scans for which in our modeling, we replaced the exponent 4 with 3 in Equation (2). They compared the relative permeabilities of hydrogen, methane, and nitrogen in fractured carbonate reservoir rock. Our work focused on the relative permeability of hydrogen.

3.2 Numerical Simulations

- Hashemi et al. (2021)

The simulation of hydrogen-brine multiphase flow in UHS at the pore scale, along with the estimation of macro-scale properties such as capillary pressure and relative permeability, was conducted using quasi-static pore network modeling (PNM). Their simulations used an open source software pnflow and was validated with experimental results for hydrocarbon reservoirs conducted. They established a base case by matching their simulation with the experiment conducted by Yekta et al. [31] under shallow conditions. They studied cyclic hysteretic multiphase flow and investigated sensitivities to contact angle and rock structure. We concentrated on the primary drainage simulations and obtained relative permeabilities for three sandstones and two carbonates rocks.

- Zhao et al. (2024)

The authors presented k_{rh} for primary drainage and imbibition processes. They simulated capillary pressure curves and relative permeabilities for five sandstones with different rock structures. One of the sandstones (S1) was investigated for the influence of wettability by using a

small and a large contact angle (26.3° and 35.8° respectively). In this study, we used the primary drainage data to run the proposed model.

Chapter 4 - Results and Discussion

In this section, we present capillary pressure curves and pore size distributions, followed by a comparison of k_{rh} estimated from the proposed model with experimentally measured results and/or numerical simulations.

4.1 Experiments

- Yekta et al. (2018)

Figures 1a–1c present results obtained under shallow reservoir conditions, while Figures 1d–1f depict results for deep reservoir conditions. The analyses were conducted using both MICP measurements and hydrogen-brine capillary pressure data. The capillary pressure curves indicate that hydrogen displaces more water at higher capillary pressures, resulting in reduced water trapping, which is more pronounced in MICP measurements. Additionally, hydrogen demonstrates a greater ability to penetrate smaller pore spaces, capturing the complexities of the rock structure and leading to a lower S_{hc}.

The pore size distributions derived from MICP suggest a broader range of pore sizes compared to those obtained from capillary pressure measurements, under both shallow and deep reservoir conditions. These findings suggest that MICP may not fully capture the intricate interactions of hydrogen within the pore network. This aligns with the findings of Boon and Hajibeygi [34], who demonstrated that the interplay between gravitational, capillary, and viscous forces can result in complex displacement patterns during (UHS). Specifically, they noted that the high density contrast between hydrogen and water can lead to gravity segregation, while capillary barriers may counteract this effect and promote hydrogen spreading.

Consequently, caution must be exercised when utilizing MICP data to characterize rock structure for hydrogen storage applications and when employing MICP-derived capillary pressure

curves to extend hydrogen-brine capillary pressure measurements, particularly at higher capillary pressures.

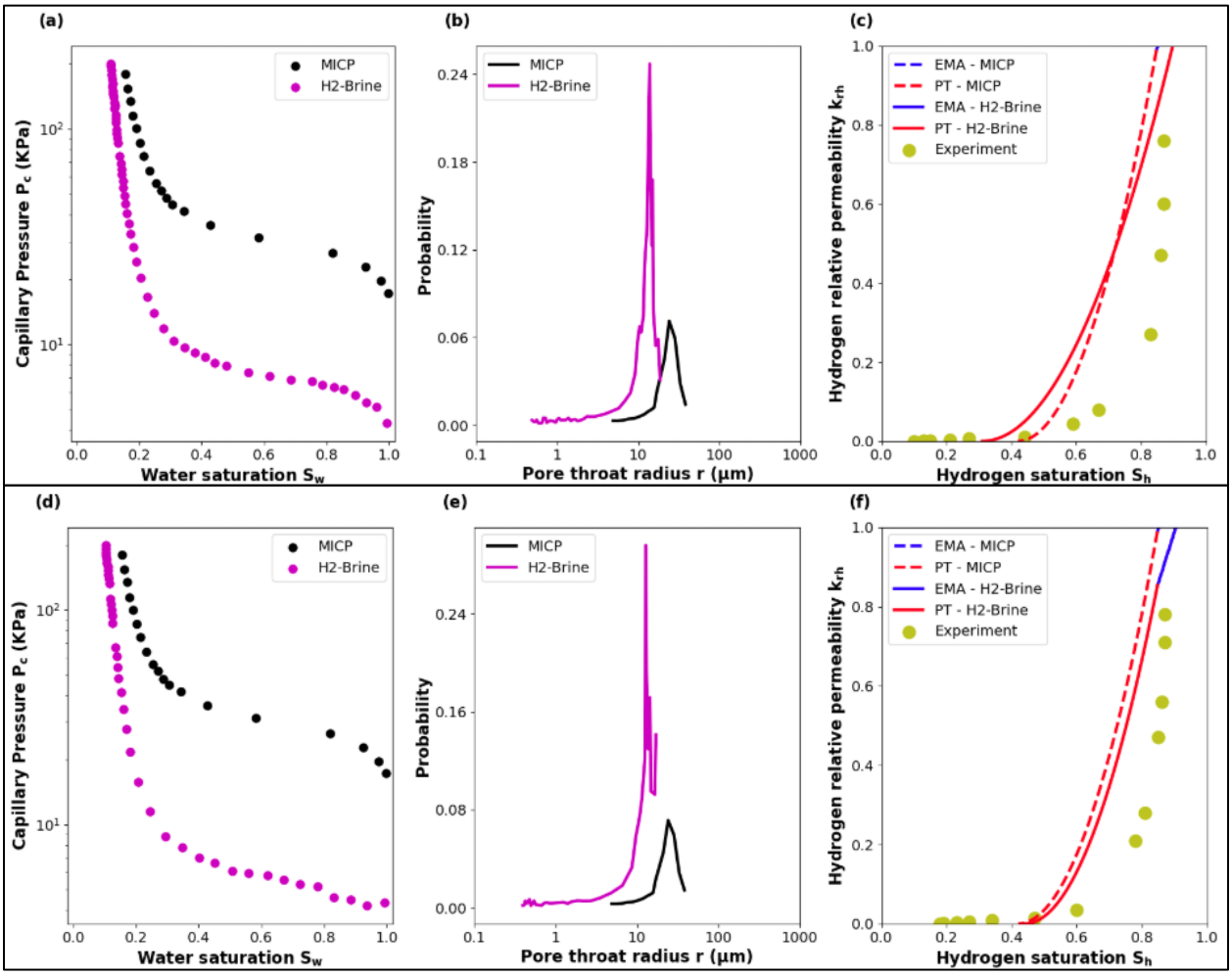

Figure 4-1 (a) Capillary pressure curves, (b) derived pore size distributions, and (c) estimated and measured relative permeability curves for the Buntsandstein sandstone sample at shallow reservoir conditions (top plots). (d) Capillary pressure curves, (e) derived pore size distributions, and (f) estimated and measured relative permeability curves at deep reservoir conditions (bottom plots).

Furthermore, Figures 1c and 1f show that k_{rh} estimated from MICP measurements are higher than those derived from hydrogen-brine capillary pressure data which is expected. The observed discrepancy between our modeled k_{rh} and those from experiment is likely due to the absence of confining pressure in our model, whereas the experimental data account for this

effect. This highlights the need for future research to incorporate confining pressure effects to enhance the accuracy of k_{rh} predictions in UHS systems.

- Rezaei et al. (2022)

Figure 2 presents the MICP curves, pore size distributions, and hydrogen relative permeability as a function of hydrogen saturation for the sandstone samples S1 (Figures a–c), S2 (Figures d–f), and C1 (Figures g–i). For the S1 sample, due to the lack of capillary pressure data and the MICP analysis not capturing trapping effects, we estimated the trapped water saturation by averaging values from the five experimental datasets (Exp1–Exp5) reported for S1. The experimental data points, plotted in distinct colors in Figure 2c, represent measurements conducted under varying salinity and pressure conditions. The results indicate that our model effectively captures the overall trend of k_{rh} with increasing saturation. However, at very low saturations, the model underestimates k_{rh} when using the critical gas saturation value of S_{hc} =0.09 obtained from the inflection point of the MICP curve. The measured S_{hc}=0.0015 provides a better match with experimental data (results not shown).

For the S2 sample, only a single experimental dataset was available, measured under 20.68 MPa pressure and 35 ppt salinity conditions (represented by the yellow data points in Figure 2f). The modeled result shows a slight shift from the measured k_{rh} with an estimated S_{hc} of 0.2. However, the measured S_{hc} =0.009 yields a more accurate estimation (results not shown).

The C1 dataset consists of a single experimental measurement on a carbonate sample under 20.68 MPa pressure and 35 ppt salinity, represented by the yellow data points in Figure 2i. Trapping effects were estimated from the measured relative permeabilities.

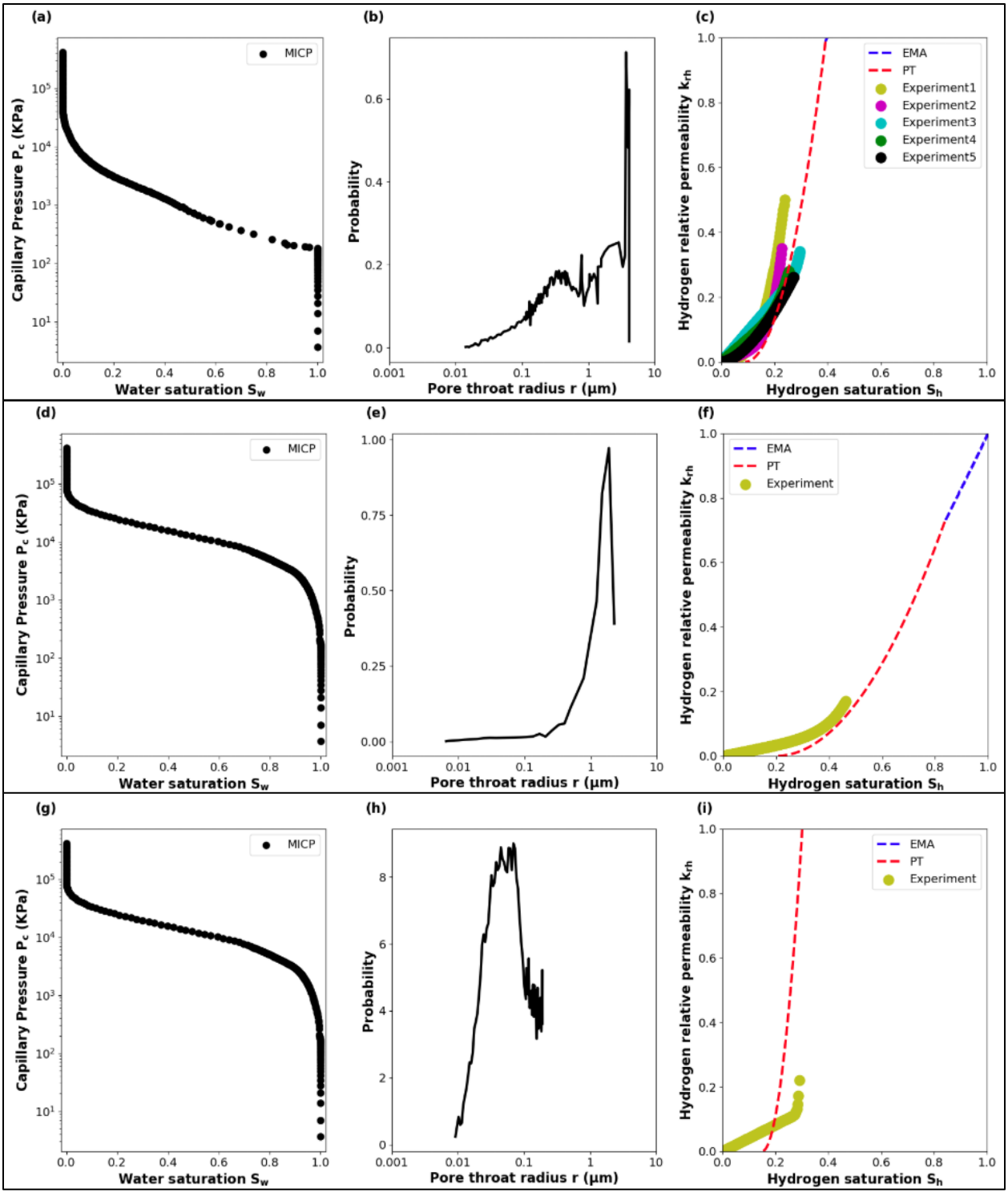

Figure 4-2 (a) Capillary pressure curves, (b) derived pore size distributions, and (c) estimated and measured relative permeability curves for S1 sandstone sample (top plots). (d) Capillary pressure curves, (e) derived pore size distributions, and (f) estimated and measured relative permeability curves for S2 sandstone sample (middle plots). (g) Capillary pressure curves, (h) derived pore size distributions, and (i) estimated and measured relative permeability curves for C1 carbonate sample (bottom plots).

The MICP curve for the C1 carbonate sample (Figure 2g) exhibits a steep increase in capillary pressure as water saturation decreases. The significantly high capillary pressures, at high water saturations, suggest that small pores dominate the system. This is further supported by the probability distribution of pore throat radii (Figure 2h), which peaks in the sub-micron range, indicating a prevalence of small pores.

However, the experimental k_{rh} curve (Figure 2i) exhibits an unusual shape, initially following a diagonal trend before transitioning abruptly into a near-vertical rise. This behavior suggests that hydrogen was gradually displacing water at lower saturations but then reached a breakthrough point or percolation threshold, where continuous gas pathways formed, leading to a sudden increase in permeability. The discrepancy between experimental and modeled results suggests that some critical flow dynamics and saturation effects are not fully captured by MICP and the theoretical model.

A likely explanation is the presence of vugs and fractures, which are common in carbonate rocks but may not be well-represented in MICP measurements. These secondary porosities can lead to non-monotonic behavior in k_{rh}, as gas may remain disconnected in isolated pore spaces before rapidly mobilizing once a critical saturation is reached. The observed deviation underscores the need for improved modeling approaches, such as dual-porosity frameworks or corrective factors tailored for carbonate reservoirs, to enhance k_{rh} predictions

- Boon & Hajibeygi (2022)

Figure 3 presents the capillary pressure curves, pore size distribution, and k_{rh} results for the Berea sandstone sample investigated by Boon and Hajibeygi [34]. To extend the capillary pressure curve over the full saturation range and determine the receding contact angle of the

H_2/brine system, the authors combined hydrogen-brine capillary pressure measurements with MICP data from a Berea sandstone core of comparable porosity and permeability, as reported by Ni et al. [38] In this study, both datasets were used separately in the k_{rh} model. The results indicate that a hydrogen critical saturation S_{hc} of 0.31, derived from the inflection point of the MICP curve, provides an accurate estimation of k_{rh}. However, due to the limited saturation range covered by the hydrogen-brine capillary pressure dataset (Figure 3a), it was unable to effectively capture the hydrogen critical saturation.

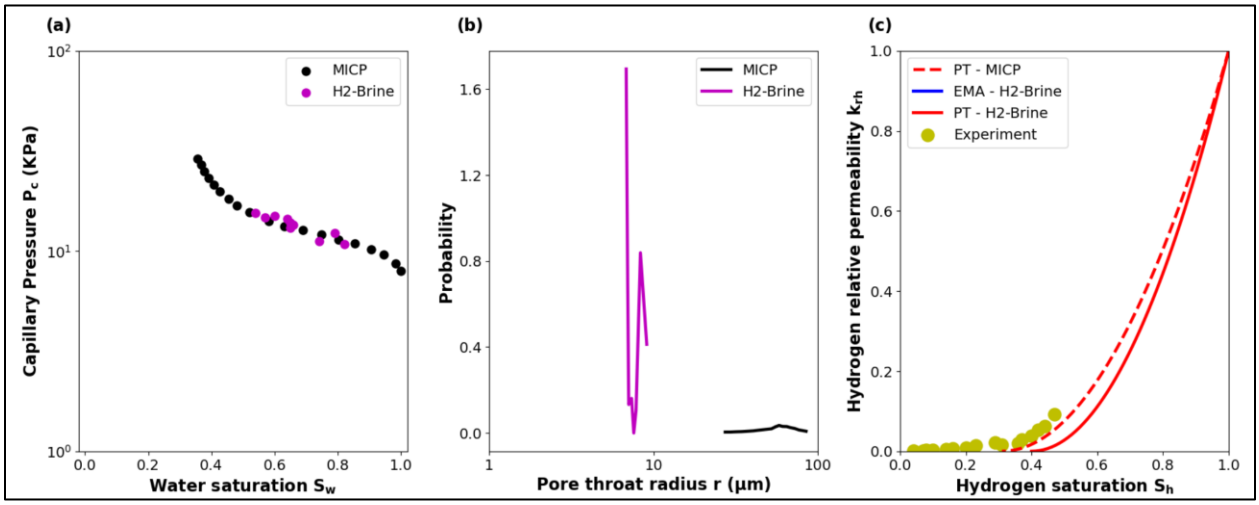

Figure 4-3 (a) Capillary pressure curves, (b) derived pore size distributions, and (c) estimated and measured relative permeability curves for the Berea (Liver) sandstone sample.

- Higgs et al. (2024)

Figure 4 illustrates the pore size distribution derived from micro-CT imaging and MICP analysis. The pore size distribution obtained from micro-CT imaging spans nearly three orders of magnitude, whereas that derived from MICP covers approximately two orders of magnitude. A hydrogen critical saturation, S_{hc} =0.31 was determined from the inflection point of the MICP curve and subsequently utilized for k_{rh} estimations. As shown in Figure 4c, the k_{rh} derived from micro-CT data is lower than that obtained from MICP analysis. This observation is expected, as micro-

CT imaging provides a more detailed representation of the pore structure, capturing its complexity more effectively. Moreover, the k_{rh} derived from micro-CT imaging exhibits better agreement with experimental measurements. However, at higher saturations, some deviation is observed, which may be attributed to the absence of contact angle considerations in the current model.

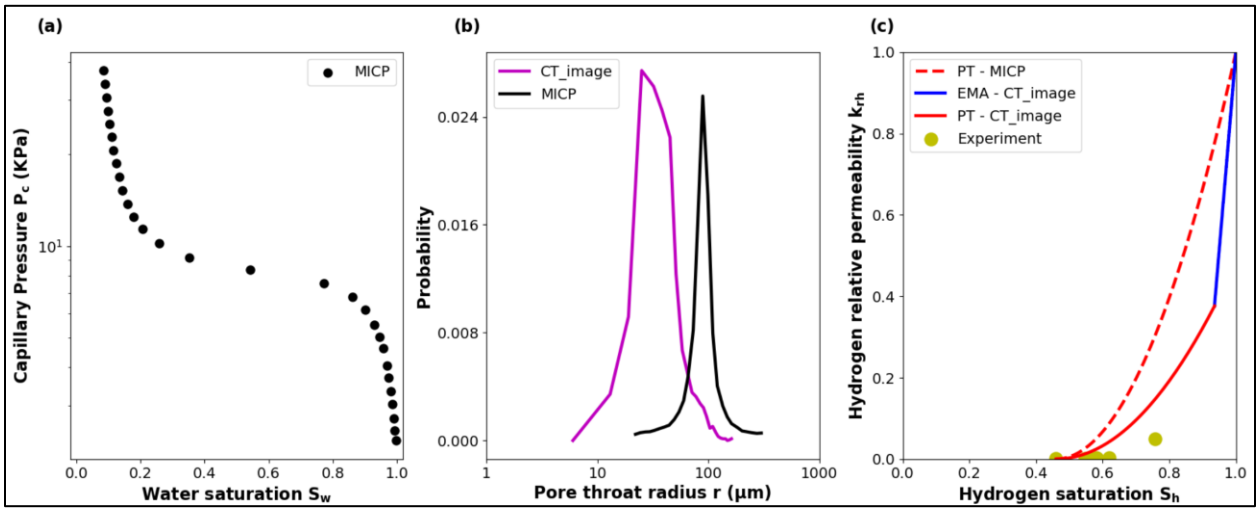

Figure 4-4 (a) Capillary pressure curves, (b) derived pore size distributions, and (c) estimated and measured relative permeability curves for the Bentheimer sandstone sample.

- Manoorkar et al. (2024)

Figure 5 shows the fracture aperture distribution for a fractured carbonate sample obtained from dry scan image. The experiment reported very low matrix porosity of <0.01 indicating that fluid transport is significantly influenced by fracture networks rather than matrix porosity alone. We used S_{hc} = 0.08 from the k_{rh} measurements for our model and found that the proposed model gives reasonable estimates.

The experimental k_{rh} aligns more closely with the PT model at low hydrogen saturations, suggesting that flow initiation and connectivity play a critical role.

The discrepancy at high S_h may be due to model assumptions that do not account for fracture-specific phenomena such as preferential flow paths, capillary pressure effects, or the transition from fracture-dominated to matrix-assisted flow.

Future work could focus on incorporating fracture connectivity models or dual-porosity approaches to better capture the full complexity of hydrogen transport in fractured systems.

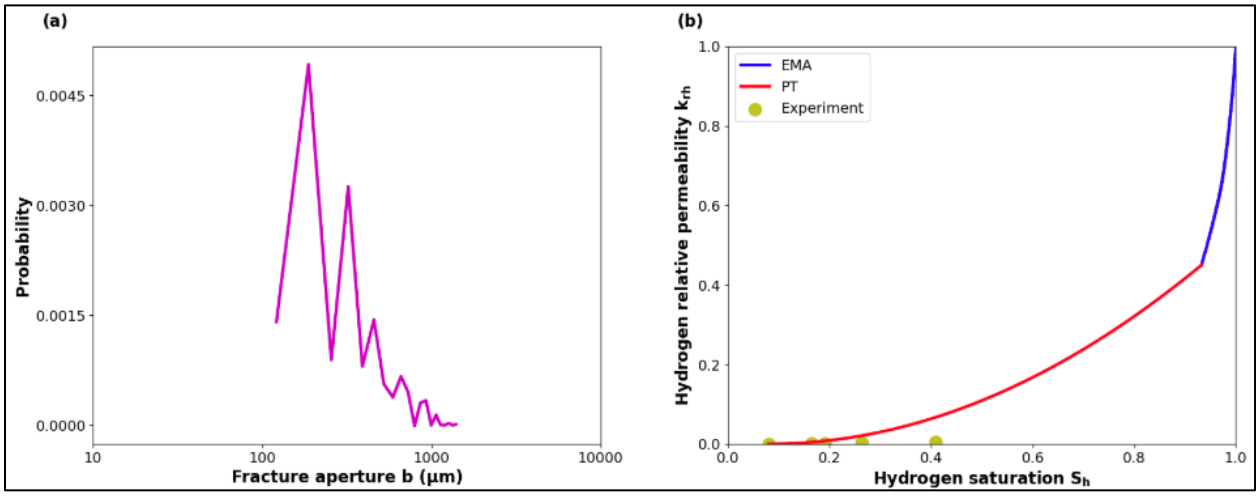

Figure 4-5 (a) Fracture aperture distribution, and (b) estimated and measured relative permeability curves for a fractured carbonate sample.

4.2 Simulations

- Hashemi et al. (2021)

Figure 6 presents the results for three sandstone samples (Figure 6a-6i) and two carbonate samples (Figure 7j-7o) simulated by Hashemi et al. [32]. The sandstone samples exhibit similar structural characteristics, particularly in terms of pore sizes, leading to similar values of S_{hc}. Our model demonstrates a strong agreement with the simulation results for the sandstones. However, discrepancies are observed in the carbonate samples, especially at intermediate saturations. These discrepancies are likely due to the effects of secondary porosity, such as vugs and fractures, as previously discussed for the carbonate sample in the work of Rezaei et al. [33].

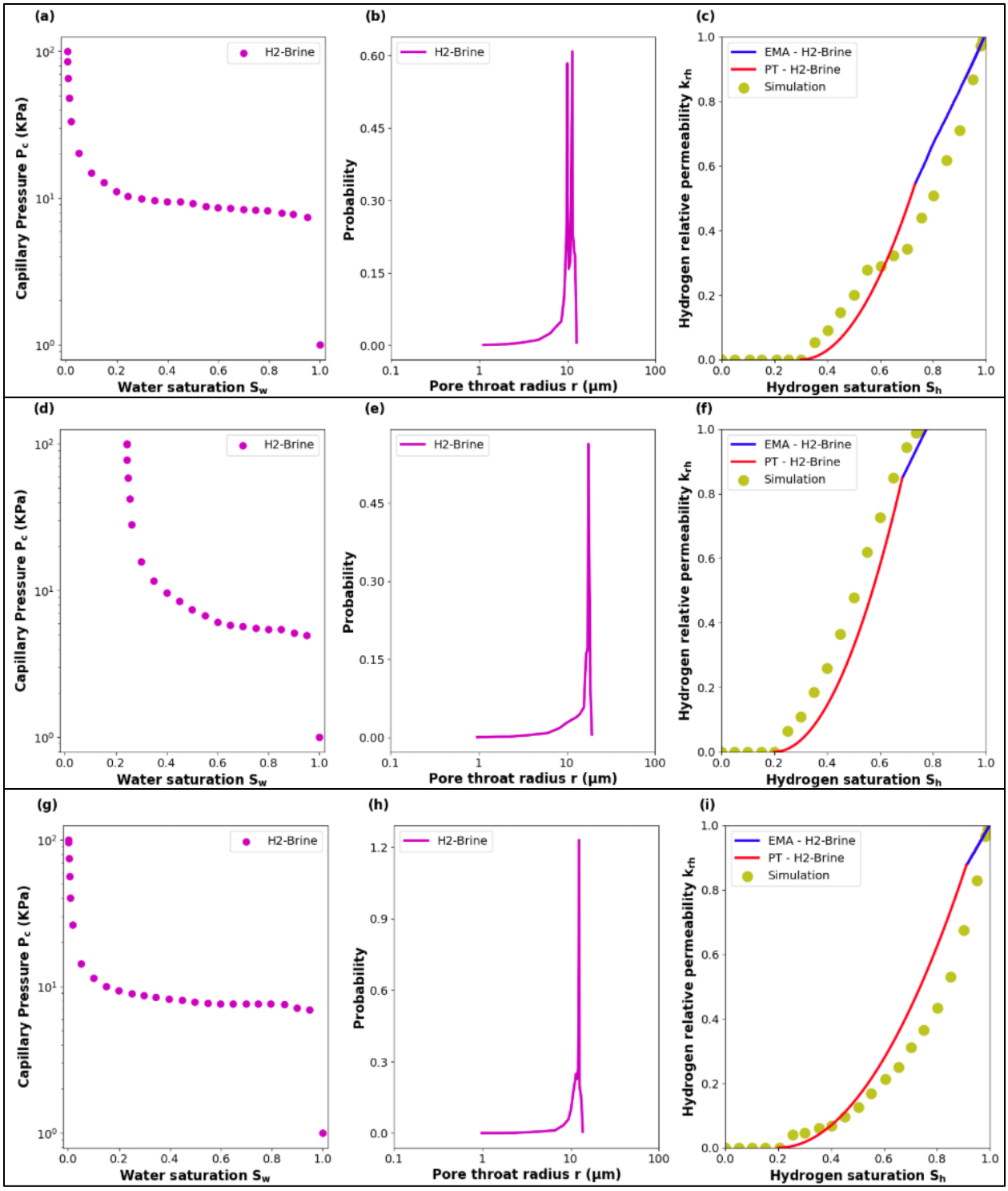

Figure 4-6 (a) Capillary pressure curves, (b) derived pore size distributions, and (c) estimated and measured relative permeability curves for Berea* sandstone sample (top plots). (d) Capillary pressure curves, (e) derived pore size distributions, and (f) estimated and measured relative permeability curves for Berea (small) sandstone sample (middle plots). (g) Capillary pressure curves, (h) derived pore size distributions, and (i) estimated and measured relative permeability curves for A1 sandstone sample (bottom plots).

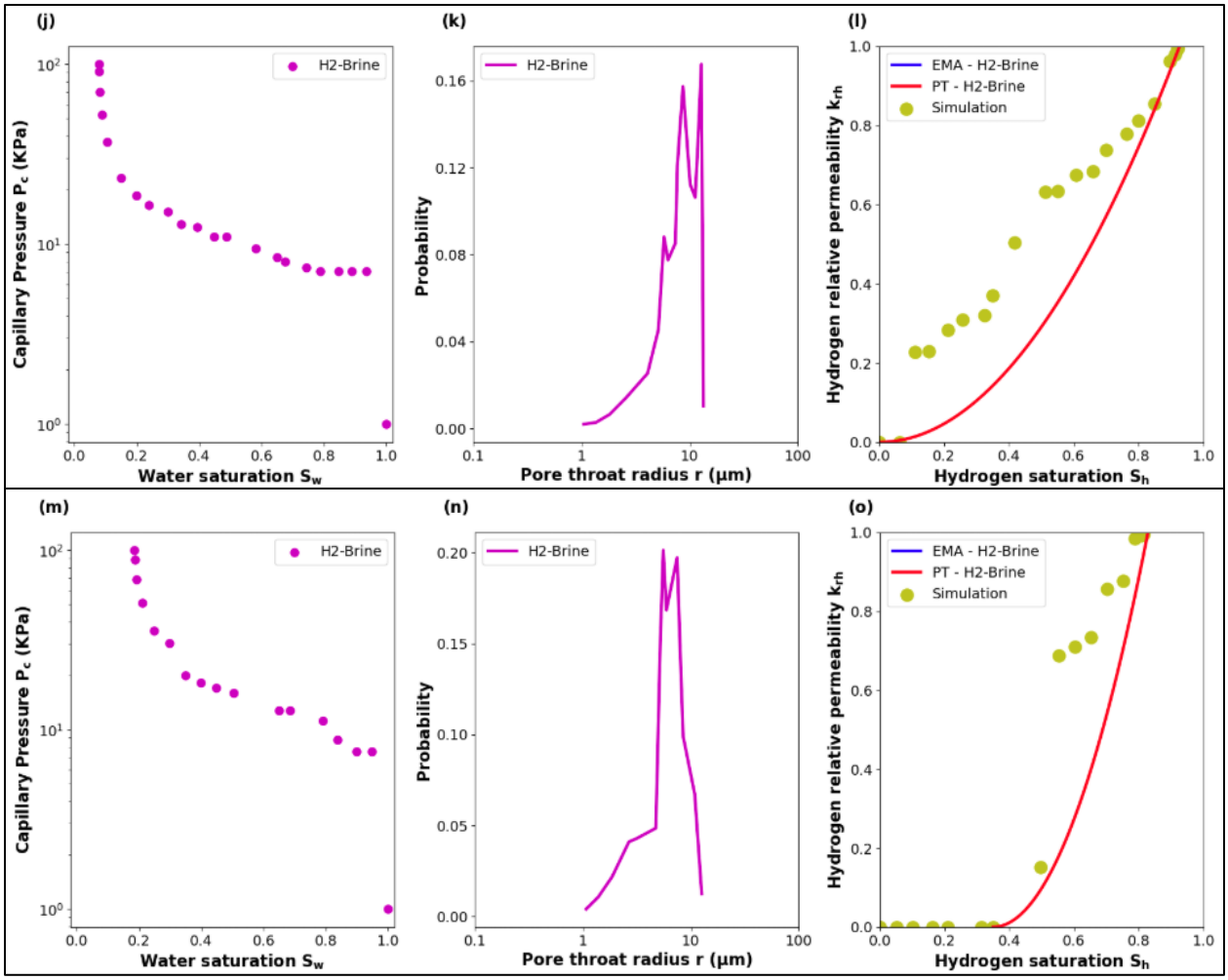

Figure 4-7 (a) Capillary pressure curves, (b) derived pore size distributions, and (c) estimated and measured relative permeability curves for C1 carbonate sample (top plots). (d) Capillary pressure curves, (e) derived pore size distributions, and (f) estimated and measured relative permeability curves C2 carbonate sample (bottom plots).

- Zhao et al. (2024)

Figure 8a–8c compares the capillary pressure curves, pore size distributions, and k_{rh} results for sample S1 with simulations conducted using a small contact angle of 26.3° and a larger contact angle of 35.8°. The differences between the two cases are minimal, likely due to the relatively small difference in contact angles. The modeled k_{rh} closely match the simulations at

high saturations but underestimate k_{rh} at lower and intermediate saturations at S_{hc} = 0.25. This trend is consistent with observations for sample S7 in Figure 9j-9l.

For samples S2 and S3, the model provides accurate estimations only at high saturations when using the estimated S_{hc}. Notably, the measured S_{hc}, presented in Table 1, yields improved estimations across all cases (results not shown). In the case of the BG sandstone, the estimated S_{hc} = 0.07, determined from the inflection point of the MICP curve, aligns with the measured S_{hc}, leading to an accurate estimation of k_{rh}. These results highlight the critical importance of accurately estimating S_{hc} for precise predictions of k_{rh} in this dataset. Also notable is that the crossover saturation from percolation theory to EMA type flow, S_{hx} is different across all samples, and the curves are dominated by percolation theory type flow for all the samples except S1 and S7.

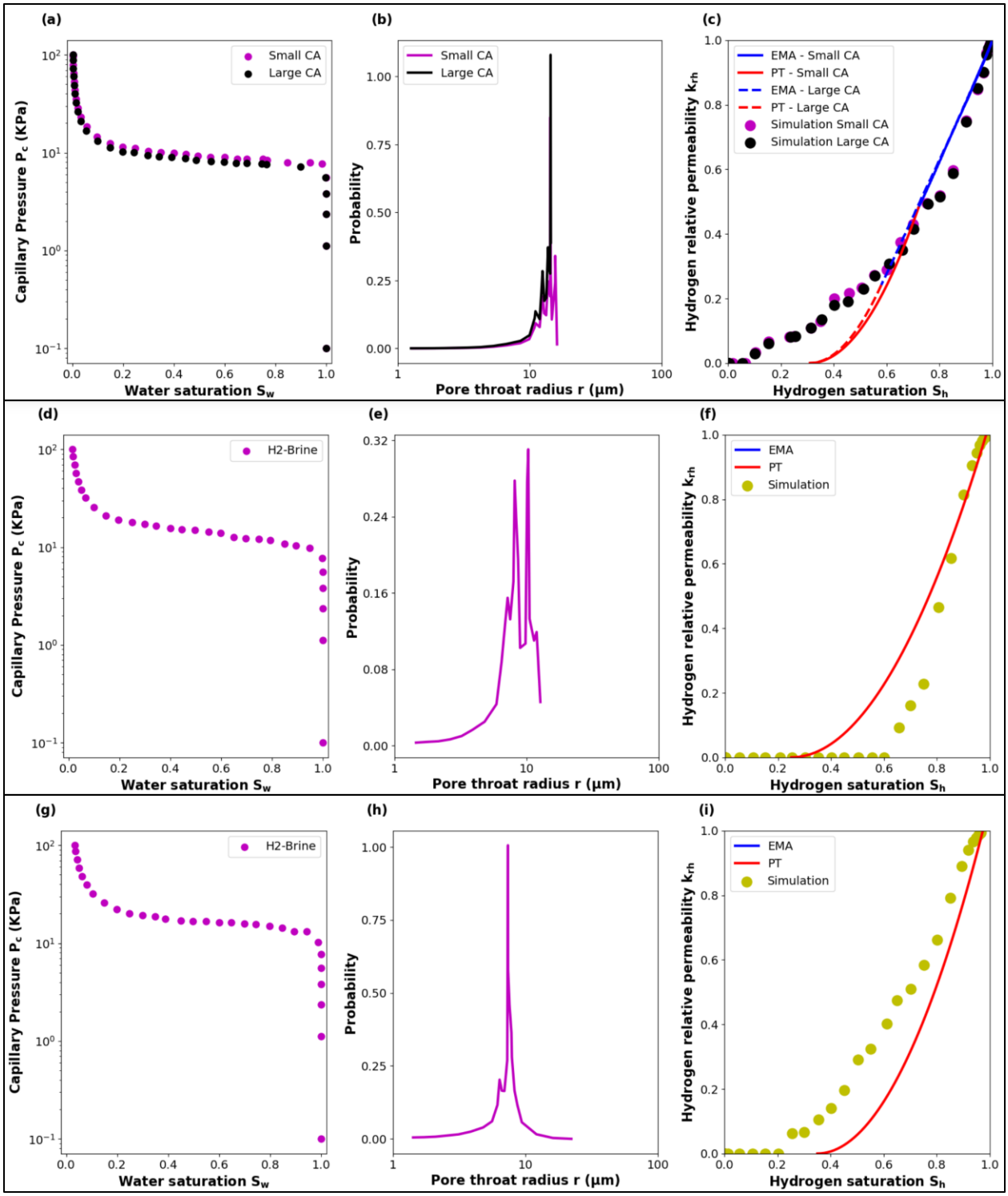

Figure 4-8 (a) Capillary pressure curves, (b) derived pore size distributions, and (c) estimated and measured relative permeability curves for S1 sandstone sample using small and large contact angles (top plots). (d) Capillary pressure curves, (e) derived pore size distributions, and (f) estimated and measured relative permeability curves for S2 sandstone sample (middle plots). (g) Capillary pressure curves, (h) derived pore size distributions, and (i) estimated and measured relative permeability curves for S3 sandstone sample (bottom plots).

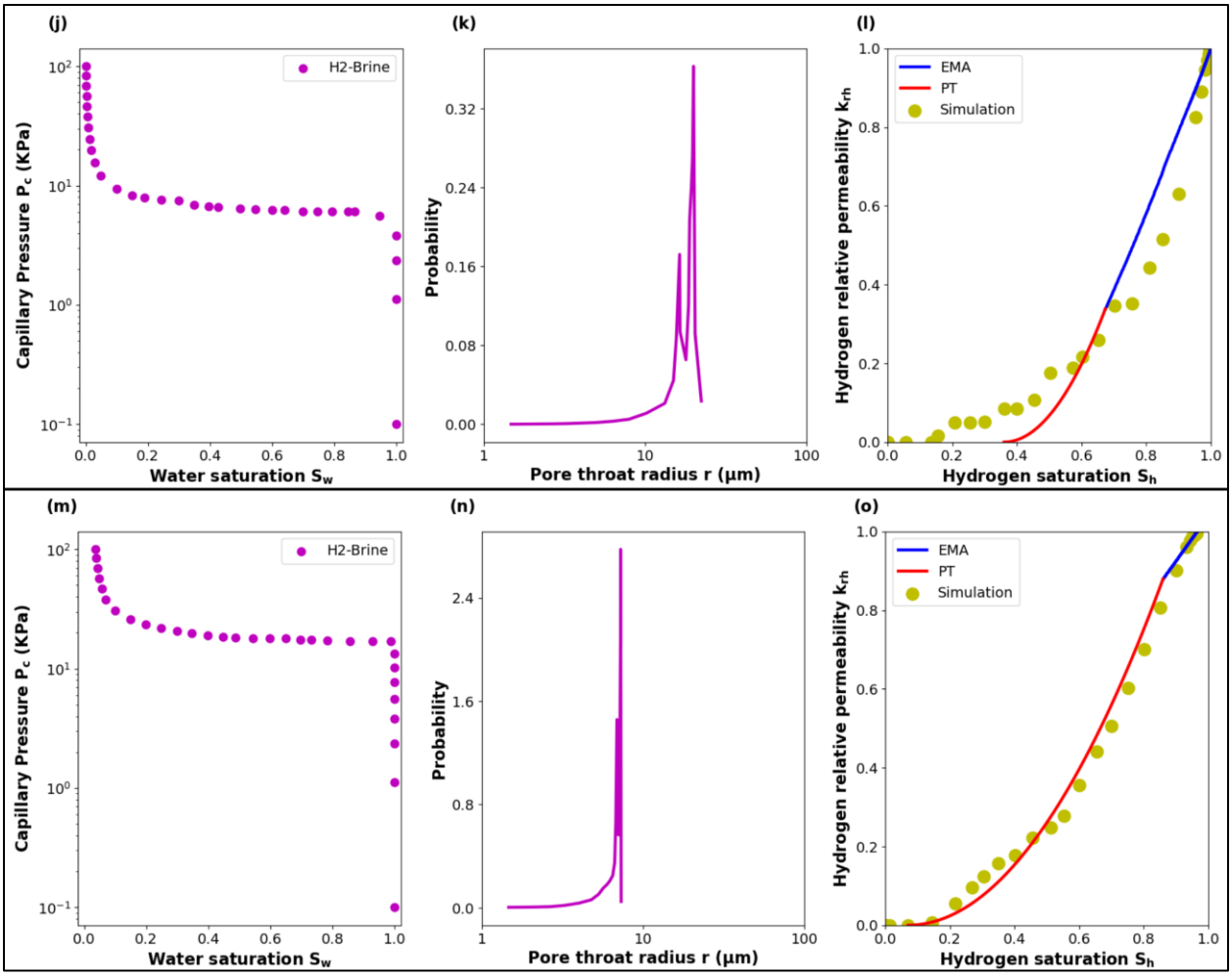

Figure 4-9 (a) Capillary pressure curves, (b) derived pore size distributions, and (c) estimated and measured relative permeability curves for S7 sandstone sample (top plots). (d) Capillary pressure curves, (e) derived pore size distributions, and (f) estimated and measured relative permeability curves for BG sandstone sample (bottom plots).

Chapter 5 - Conclusions

This study utilized concepts from the effective-medium approximation (EMA) and universal power-law scaling derived from percolation theory (PT) to develop a theoretical model for hydrogen relative permeability, k_{rh} in potential reservoir rocks. We assumed that hydraulic flow primarily governs gas transport. Our proposed model calculates k_{rh} based on pore space characteristics, including pore size distribution, and pore connectivity (as indicated by critical hydrogen saturation). Critical hydrogen saturation was derived from the inflection point of MICP curves. We assessed the validity of our theoretical approach by comparing the model's estimations with eight experimental measurements and eleven pore-network simulations from existing literature. The results indicated that k_{rh} was estimated reasonably well except for certain carbonate rocks, which may possess secondary porosities (e.g., vugs and fractures), and two sandstone samples, which were improved by using measured critical saturations emphasizing the need for accurate S_{hc} estimation. We also observed that S_{hx} is non-universal and that most of the rocks considered were mostly dominated by percolation theory type flow of hydrogen.

References

[1] Dopffel N, Jansen S, Gerritse J. Microbial side effects of underground hydrogen storage – Knowledge gaps, risks and opportunities for successful implementation. Int J Hydrogen Energy 2021;46:8594–606. https://doi.org/10.1016/j.ijhydene.2020.12.058.

[2] Iglauer S, Ali M, Keshavarz A. Hydrogen Wettability of Sandstone Reservoirs: Implications for Hydrogen Geo-Storage. Geophys Res Lett 2021;48. https://doi.org/10.1029/2020GL090814.

[3] Sambo C, Dudun A, Samuel SA, Esenenjor P, Muhammed NS, Haq B. A review on worldwide underground hydrogen storage operating and potential fields. Int J Hydrogen Energy 2022;47:22840–80. https://doi.org/10.1016/j.ijhydene.2022.05.126.

[4] Winkler-Goldstein R, Rastetter A. Power to gas: The final breakthrough for the hydrogen economy? Green 2013;3:69–78. https://doi.org/10.1515/green-2013-0001.

[5] Kanaani M, Sedaee B, Asadian-Pakfar M. Role of Cushion Gas on Underground Hydrogen Storage in Depleted Oil Reservoirs. J Energy Storage 2022;45:103783. https://doi.org/10.1016/j.est.2021.103783.

[6] Lysyy M, Fernø M, Ersland G. Seasonal hydrogen storage in a depleted oil and gas field. Int J Hydrogen Energy 2021;46:25160–74. https://doi.org/10.1016/j.ijhydene.2021.05.030.

[7] Wang G, Pickup G, Sorbie K, Mackay E. Scaling analysis of hydrogen flow with carbon dioxide cushion gas in subsurface heterogeneous porous media. Int J Hydrogen Energy 2022;47:1752–64. https://doi.org/10.1016/j.ijhydene.2021.10.224.

[8] Krevor SCM, Pini R, Zuo L, Benson SM. Relative permeability and trapping of CO2 and water in sandstone rocks at reservoir conditions. Water Resour Res 2012;48. https://doi.org/10.1029/2011WR010859.

[9] Müller N. Supercritical CO2-Brine Relative Permeability Experiments in Reservoir Rocks-Literature Review and Recommendations. Transp Porous Media 2011;87:367–83. https://doi.org/10.1007/s11242-010-9689-2.

[10] Lenhard RJ, Parker JC, Mishra S. Measurement and prediction of saturation-pressure relationships in three-phase porous media systems. J Contam Hydrol 1987.

[11] Corey AT. The interrelation between gas and oil relative permeabilities. Producers Monthly 1954;19:38–41.

[12] Brooks R, Corey A. Hydraulic properties of porous media. Hydrology Paper No 3 1964:27 pages.

[13] Bo Z, Boon M, Hajibeygi H, Hurter S. Impact of experimentally measured relative permeability hysteresis on reservoir-scale performance of underground hydrogen storage (UHS). Int J Hydrogen Energy 2023;48:13527–42. https://doi.org/10.1016/j.ijhydene.2022.12.270.

[14] Feldmann F, Hagemann B, Ganzer L, Panfilov M. Numerical simulation of hydrodynamic and gas mixing processes in underground hydrogen storages. Environ Earth Sci 2016;75. https://doi.org/10.1007/s12665-016-5948-z.

[15] Van Genuchten MTh. A closed-form equation for predicting the hydraulic conductivity of unsaturated soils. Soil Science Society of America Journal 1980;44.5:892–8.

[16] Dury O, Fischer U, Schulin R. A comparison of relative nonwetting-phase permeability models. Water Resour Res 1999;35:1481–93. https://doi.org/10.1029/1999WR900019.

[17] Parker JC, Lenhard RJ, Kuppusamy T. A Parametric Model for Constitutive Properties Governing Multiphase Flow in Porous Media. vol. 23. 1987.

[18] Zheng Z, Ma Q, Hu P, Song Y, Wang D. Uncertainty and sensitivity analysis of relative permeability curves for the numerical simulation of CO2 core flooding. Greenhouse Gases: Science and Technology 2020;10:519–30. https://doi.org/10.1002/ghg.1977.

[19] Ogolo NA, Ezeaneche OS, Onyekonwu MO. The Comparison of Experimental Relative Permeability Data with Corey's Model Results: A Case Study. Journal of Oil, Gas and Petrochemical Technology 2023;10:25–34. https://doi.org/10.22034/jogpt.2023.355385.1106.

[20] Picchi D, Battiato I. The Impact of Pore-Scale Flow Regimes on Upscaling of Immiscible Two-Phase Flow in Porous Media. Water Resour Res 2018;54:6683–707. https://doi.org/10.1029/2018WR023172.

[21] Ghanbarian B, Liang F, Liu HH. Modeling gas relative permeability in shales and tight porous rocks. Fuel 2020;272. https://doi.org/10.1016/j.fuel.2020.117686.

[22] Ghanbarian B, Javadpour F. Upscaling pore pressure-dependent gas permeability in shales. J Geophys Res Solid Earth 2017;122:2541–52. https://doi.org/10.1002/2016JB013846.

[23] Richesson S, Sahimi M. Hertz-Mindlin Theory of Contacting Grains and the Effective-Medium Approximation for the Permeability of Deforming Porous Media. Geophys Res Lett 2019;46:8039–45. https://doi.org/10.1029/2019GL083727.

[24] Lindquist WB, Venkatarangan A, Dunsmuir J, Wong TF. Pore and throat size distributions measured from synchrotron X-ray tomographic images of Fontainebleau sandstones. J Geophys Res Solid Earth 2000;105:21509–27. https://doi.org/10.1029/2000jb900208.

[25] Seaton NA. Determination of the connectivity of porous solids from nitrogen sorption measurements. Chem Eng Sci 1991;46:1895–909. https://doi.org/10.1016/0009-2509(91)80151-N.

[26] Hunt A, Ewing R, Ghanbarian B. Percolation theory for flow in porous media (Vol. 880). Springer. vol. 880. Springer; 2014.

[27] Sahimi M. Flow and Transport in Porous Media and Fractured Rock. Wiley; 2011. https://doi.org/10.1002/9783527636693.

[28] Zare Sourmanabad M, Norouzi S, Mirzaei F, Yokeley BA, Ebrahimian H, Ghanbarian B. A percolation model of unsaturated hydraulic conductivity using three-parameter Weibull distribution. Adv Water Resour 2024;188. https://doi.org/10.1016/j.advwatres.2024.104696.

[29] Fredlund DG, Xing A. Equations for the soil-water characteristic'curve ' i ? vol. 31. 1994.

[30] Levine S, Cuthiell DL. Relative Permeabilitties in Two-Phase Flow Through Porous Media: an Application of Effective Medium Theory. Journal of Canadian Petroleum Technology 1986;25. https://doi.org/10.2118/86-05-10.

[31] Yekta AE, Manceau JC, Gaboreau S, Pichavant M, Audigane P. Determination of Hydrogen–Water Relative Permeability and Capillary Pressure in Sandstone: Application to Underground Hydrogen Injection in Sedimentary Formations. Transp Porous Media 2018;122:333–56. https://doi.org/10.1007/s11242-018-1004-7.

[32] Hashemi L, Blunt M, Hajibeygi H. Pore-scale modelling and sensitivity analyses of hydrogen-brine multiphase flow in geological porous media. Sci Rep 2021;11. https://doi.org/10.1038/s41598-021-87490-7.

[33] Rezaei A, Hassanpouryouzband A, Molnar I, Derikvand Z, Haszeldine RS, Edlmann K. Relative Permeability of Hydrogen and Aqueous Brines in Sandstones and Carbonates at Reservoir Conditions. Geophys Res Lett 2022;49. https://doi.org/10.1029/2022GL099433.

[34] Boon M, Hajibeygi H. Experimental characterization of H 2 /water multiphase flow in heterogeneous sandstone rock at the core scale relevant for underground hydrogen storage (UHS). Sci Rep 2022;12. https://doi.org/10.1038/s41598-022-18759-8.

[35] Higgs S, Wang Y Da, Sun C, Ennis-King J, Jackson SJ, Armstrong RT, et al. Direct measurement of hydrogen relative permeability hysteresis for underground hydrogen storage. Int J Hydrogen Energy 2024;50:524–41. https://doi.org/10.1016/j.ijhydene.2023.07.270.

[36] Zhao Q, Wang H, Chen C. Underground hydrogen storage: A recovery prediction using pore network modeling and machine learning. Fuel 2024;357. https://doi.org/10.1016/j.fuel.2023.130051.

[37] Manoorkar S, Pakkaner GK, Omar H, Barbaix S, Ceursters D, Lathinis M, et al. From underground natural gas to hydrogen storage in fractured reservoir rock : comparing relative permeabilities for hydrogen versus methane and nitrogen 2024.

[38] Ni H, Boon M, Garing C, Benson SM. Predicting CO2 residual trapping ability based on experimental petrophysical properties for different sandstone types. International Journal of Greenhouse Gas Control 2019;86:158–76. https://doi.org/10.1016/j.ijggc.2019.04.024.